Research Square

Preprints are preliminary reports that have not undergone peer review.
They should not be considered conclusive, used to inform clinical practice,
or referenced by the media as validated information.

Machine-Learning-Guided Prediction and Process Optimization of AgCuTi/WCu Wetting with SHAP-Based Feature Interpretation

Xingxing Wang

wangxingxing@ncwu.edu.cn

North China University of Water Resources and Electric Power

Research Article

Keywords: Ag-Cu-Ti, W-Cu, Equivalent Contact Angle, SHAP, Reactive Wetting

Posted Date: November 25th, 2026

DOI: https://doi.org/10.21203/rs.3.rs-11199004/v1

License: This work is licensed under a Creative Commons Attribution 4.0 International License.
Read Full License

Machine-Learning-Guided Prediction and Process Optimization of AgCuTi/WCu Wetting with SHAP-Based Feature Interpretation

Xinmei Zhang[a], XingXing Wang[a*], Shuai Wang[a], Jianjun Shi[a], Huawei Sun[b], ZhiPeng Yuan[a]

[a]Henan International Joint Laboratory of High-efficiency Special Green Welding, North China University of Water Resources and Electric Power, Zhengzhou 450045, PR China;

[b]China Academy of Machinery Zhengzhou Research Institute of Mechanical Engineering Co.,Ltd, Zhengzhou 450001, PR China;

[*]Corresponding authors. E-mail address: wangxingxing@ncwu.edu.cn(X. Wang)

Abstract: Reliable control of AgCuTi wetting on WCu substrates is critical for electronic packaging and high-heat-flux thermal management applications. Because temperature, Ti content, and surface texture interact nonlinearly, high-temperature experiments are costly and final surface morphology cannot be known during process selection. This study therefore develops a two-stage machine-learning framework that separates process optimization from final-state interpretation. In Stage I, 125 experiments were generated using a three-factor, five-level full-factorial design, with temperature, Ti content, and nominal roughness as inputs and equivalent contact angle as the target. Among eight regression models, SVR-RBF achieved the best performance, with a 10-fold OOF (R^2) of 0.9403 and RMSE of 1.1668°, and a held-out test (R^2) of 0.9447 and RMSE of 1.217°. The optimized model screened 37,572 candidate conditions and identified 10 representative conditions, whose experimental validation yielded an MAE of 0.5513°, RMSE of 0.6319°, and (R^2) of 0.9105. In Stage II, the 10 validation samples were combined with the original data to form 135 samples with seven features. GBR achieved the best validation performance and yielded (R^2=0.9214), RMSE = 1.206°, and MAE = 0.828° on the held-out test set. SHAP analysis showed that the three process variables accounted for 70.31% of the total contribution, while post-wetting morphology provided complementary information. Overall, Stage I enables forward process optimization, whereas Stage II offers correlation-based interpretation of the final wetting state rather than causal mechanistic evidence.

Keywords: Ag-Cu-Ti; W-Cu; Equivalent Contact Angle; SHAP; Reactive Wetting

1. Introduction

WCu composites combine the low coefficient of thermal expansion and high-temperature stability of W with the high thermal and electrical conductivity of Cu. They are therefore widely used as heat spreaders, heat-dissipation substrates, electrodes, lead transitions, and dissimilar-material joining components in high-power electronic packaging, power semiconductor modules, RF and microwave devices, high-heat-flux thermal management systems, and thermoelectric systems. In these applications, WCu often serves as a critical interfacial material between heat-generating components and heat-dissipation structures. In addition to carrying and transferring heat, it must accommodate the thermal-expansion mismatch between WCu and materials such as Si, SiC, GaN, and Cu, thereby reducing thermally induced interfacial stresses and the associated risk of failure during service. Particularly in high-power, high-frequency, and high-heat-flux devices, heat generated during chip operation must be rapidly transferred through the brazed interface to the WCu heat-spreading layer or heat-dissipation structure. Consequently, the continuity of the brazed joint, interfacial bonding quality, and thermal resistance directly affect heat-dissipation efficiency, temperature distribution, and long-term device reliability. In thermoelectric devices and other systems requiring stable interfacial heat transfer, insufficient wetting may also produce unbonded regions, pores, and localized high-thermal-resistance zones, resulting in heat-flow concentration

and local temperature rises. Therefore, achieving good wetting of WCu surfaces and forming uniform, low-defect brazed interfaces are essential for the reliable application of WCu composites in high-heat-flux thermal management and electronic packaging [1-5].

AgCuTi active brazing alloys are attractive for joining WCu and other poorly wetting materials because of their relatively low liquidus temperature, good ductility, and the interfacial activation provided by Ti. For power semiconductor packaging and high-heat-flux heat-dissipation structures, improved filler-metal spreading facilitates the formation of continuous heat-transfer pathways and reduces interfacial voids and unbonded regions [6, 7]. For dissimilar-material joints such as WCu/Si, WCu/SiC, and WCu/Cu, the reactive role of Ti can further improve interfacial bonding between the filler metal and substrate. However, Ti-free AgCu melts generally exhibit poor wettability on W and WCu substrates, whereas the addition of Ti can substantially modify the solid–liquid interfacial energy through adsorption, disruption of surface oxide films, promotion of substrate dissolution, and formation of reaction layers, thereby strongly affecting filler-metal spreading and the resulting interfacial structure. Thus, for practical electronic-packaging and thermal-management components, Ti content determines not only whether wetting can occur, but may also influence reaction-layer formation, interfacial integrity, heat-transfer performance, and the service reliability of the brazed joint [8-13].

However, because multiple factors are coupled simultaneously, the reactive wetting response of the WCu/AgCuTi system is difficult to predict accurately using conventional one-factor-at-a-time approaches. Brazing temperature affects not only melt viscosity and flowability but also diffusion, substrate dissolution, elemental evaporation, and interfacial reaction kinetics. Ti content controls the degree of interfacial activation and further influences the amount, morphology, and continuity of reaction products. Surface roughness, meanwhile, changes the actual contact area and may introduce direction-dependent contact-line pinning barriers. For practical high-heat-flux electronic-packaging interfaces, these factors collectively determine whether the filler metal can spread sufficiently, whether the interface remains continuous, and whether localized defects develop. Their effects therefore do not necessarily follow simple monotonic trends [14-17]. For example, insufficient Ti or temperature may result in inadequate interfacial activation and poor wetting, whereas excessive reaction may consume active Ti, thicken the reaction layer, or impede liquid flow. Likewise, the Wenzel relationship describes only an idealized limit for the effect of roughness on apparent wetting. On actual WCu surfaces, oxide films, reaction products, anisotropic textures, and local contact-line pinning can modify or even reverse the apparent wetting advantage associated with increasing roughness. Consequently, the wetting response exhibits pronounced nonlinearity and strong process-parameter interactions, and this complexity is directly relevant to the interfacial integrity, thermal resistance, and service reliability of practical brazed joints. Accordingly, developing a wetting-prediction and process-optimization approach that simultaneously considers temperature, Ti content, and surface roughness is important for identifying low-contact-angle, high-spreadability processing windows suitable for high-power electronic packaging and high-heat-flux thermal-management components [18, 19].

Data availability and feature chronology further constrain the prediction problem. High-temperature sessile-drop experiments and three-dimensional confocal measurements are both time- and resource-intensive, making the current database relatively small compared with the number of possible process combinations. The original factors were sampled at discrete levels, whereas design-space optimization requires interpolation and limited extrapolation between these levels. In addition, the equivalent contact angle summarizes an irregular final geometry, while descriptors such as root-mean-square roughness, profile skewness, anisotropy index, and volume proxy can only be measured after wetting. These features can improve post hoc interpretation but cannot reasonably be treated as forward-looking process variables. If model selection, held-out validation, and interpretation are methodologically separated, machine learning (ML) is well suited to learning the nonlinear response under these constraints [6, 7,

20].

Against this background, this study develops a two-stage framework specifically aligned with the experimental decision-making problem. Stage I uses only controllable process variables to compare eight regression models, identify a robust predictor, search an expanded design space, and experimentally validate ten recommended conditions. Stage II incorporates these ten newly prepared samples to establish a 135-sample database, removes redundant morphology descriptors through correlation-based screening, compares four representative algorithms using an internal training–validation–test split, and applies SHAP to the selected model. The objectives are to (i) predict the equivalent contact angle using quantified internal generalization performance, (ii) identify a low-contact-angle process window while maintaining coverage of temperature and composition, and (iii) determine which controllable process variables and final-state features contribute to the fitted model, without interpreting these statistical associations as independent causal evidence [21].

2. Experimental Details

WCu/AgCuTi brazing couples were used to investigate the wetting behavior. The WCu substrates were machined into 15 mm × 15 mm × 2 mm specimens by wire electrical discharge machining and subsequently subjected to surface pretreatment. AgCuTi brazing filler metal was prepared by vacuum atomization in the form of 300-mesh powder. Brazing was conducted under vacuum using a programmed heating schedule. The specimens were heated at a rate of 10 °C/min, held at 400 °C and 700 °C, respectively, and then heated to the designated brazing temperature of 850–930 °C, where they were held for 10 min before furnace cooling.

Table 1. Descriptive statistics for the initial 125-sample database.

Feature	Unit	Minimum	Mean	Standard deviation	Maximum
Equivalent contact angle	°	5.806	14.42	4.89	29.01
Temperature	°C	850	890	28.4	930
Ti content	wt.%	2	3	0.71	4
Nominal roughness	μm	0.075	0.505	0.5204	1.5
RMS roughness	a.u.	3.289	15.2	6.981	39.4
Profile skewness	–	−4.495	−0.328	0.9548	1.029
Anisotropy index	–	2.033	2.226	0.2307	3.175
Volume proxy	voxel	1.004×10^7	2.508×10^7	1.37×10^7	9.785×10^7

A 5 × 5 × 5 full-factorial design was employed, with brazing temperature, Ti content, and nominal roughness as the three experimental factors, yielding a total of 125 independent experimental conditions. The brazing temperatures were set at 850, 870, 890, 910, and 930 °C; the Ti contents were 2.0, 2.5, 3.0, 3.5, and 4.0 wt.%; and the nominal roughness values were 0.075, 0.15, 0.30, 0.50, and 1.50 μm.

After brazing, a KC-X3000 series three-in-one precision measuring microscope (Keyence) was used to acquire the three-dimensional surface height matrix and two-dimensional projected images of the droplets. The

droplet region was segmented from the projected image, and the equivalent circular radius was determined from the projected area. Combined with the measured droplet volume, the equivalent contact angle was calculated using a spherical-cap model and adopted as the response variable characterizing the final wetting state.

In addition, several surface morphology descriptors were extracted from the three-dimensional height matrix, including root-mean-square roughness, profile skewness, anisotropy index, volume proxy, height range, and profile kurtosis, as listed in Table 1. Because these descriptors were obtained only after wetting, they were used exclusively to characterize the final surface state and were not treated as controllable process inputs available before the experiment.

Before model development, the dataset was examined for missing values, duplicate records, and outliers. Pearson and Spearman correlation analyses were subsequently performed to characterize the linear and monotonic relationships among the variables.

3. Machine Learning Procedure

The machine-learning procedure was divided into two stages, as illustrated in Fig. 1. In Stage I, an SVR-RBF model based on three controllable process parameters—temperature, Ti content, and nominal roughness—was developed to predict the equivalent contact angle and subsequently identify a low-contact-angle process window characterized by moderate Ti content, an appropriate brazing temperature, and low-to-moderate surface roughness. Experimental validation confirmed that the process parameters accounted for the major variations in wetting behavior; however, the remaining prediction deviations indicated that the actual wetting response was also influenced by the final surface state formed during wetting. Therefore, after process optimization, the newly validated samples and their post-wetting three-dimensional surface morphology were further incorporated into the analysis, extending the focus from process-condition prediction to final wetting-state interpretation.

Accordingly, Stage II established a GBR model incorporating both the process parameters and final surface morphology descriptors, and subsequently employed SHAP analysis to quantify the relative contributions of individual features. This stage was intended to further elucidate the statistical associations between processing conditions, the resulting surface morphology, and the equivalent contact angle, thereby providing a complementary interpretation of the wetting response beyond forward process prediction.

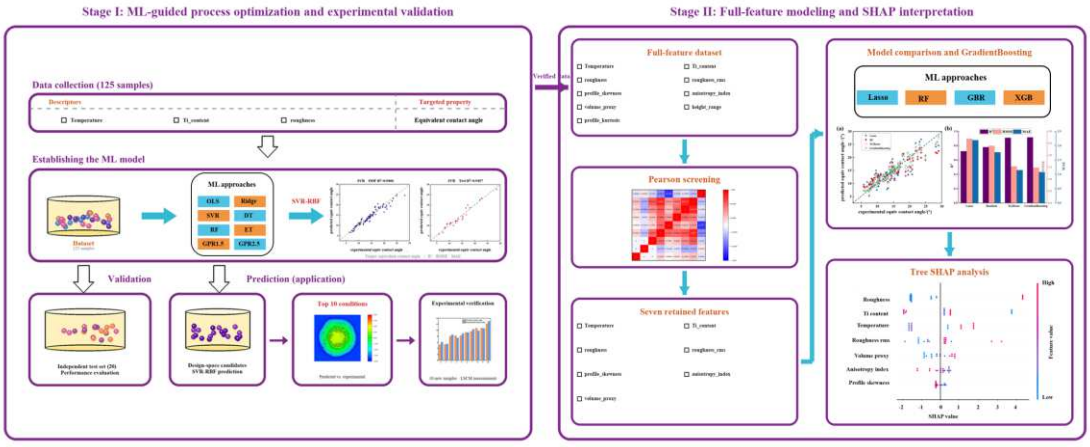

Figure 1. Two-stage workflow for ML-guided process optimization, experimental validation, and SHAP interpretation using 135 samples and seven retained features.

3.1 Stage I

After establishing the complete experimental database and obtaining the equivalent contact angles, Stage I machine-learning models were first developed to further characterize the nonlinear relationship between process parameters and wetting performance and to facilitate the transition from experimental characterization to process optimization. This stage followed the workflow of "model development–performance evaluation–optimal model selection–process-space search–experimental validation." Only the three controllable process parameters available prior to experimentation—temperature, Ti content, and nominal roughness—were used as input variables, with equivalent contact angle as the prediction target. This design ensured that the resulting model retained practical applicability for forward process prediction and optimization.

Specifically, the 125 experimental datasets were randomly divided into 80% training and 20% independent test sets. Within the training set, 10-fold cross-validation was employed for model evaluation and hyperparameter optimization to reduce the influence of a single data split on performance assessment. Eight regression models were compared: ordinary least squares (OLS), second-order polynomial ridge regression (Ridge-Poly2), support vector regression with a radial basis function kernel (SVR-RBF), decision tree (DT), random forest (RF), extremely randomized trees (ET), and two Gaussian process regression (GPR) models with different Matérn kernels. For models requiring feature scaling, standardization was incorporated into the modeling pipeline, and model hyperparameters were optimized using grid search. Model performance was evaluated using R^2, RMSE, and MAE, which characterize goodness of fit and prediction error, while out-of-fold (OOF) predictions generated during cross-validation were used to assess model stability. After model selection, the optimal model was retrained using the complete training set and subsequently evaluated on the independent test set, which had not been involved in model selection, thereby providing a more reliable assessment of its generalization performance.

The best-performing SVR-RBF model was then applied to predict the equivalent contact angle across an expanded continuous process-design space beyond the original 125 discrete experimental points. By extending the search ranges of temperature, Ti content, and nominal roughness, an expanded design space containing 37,572 candidate process combinations was constructed, and the predicted equivalent contact angle was calculated for each condition. The candidate conditions were subsequently ranked according to their predicted contact angles, while prediction performance, coverage of the process space, and experimental feasibility were considered simultaneously to avoid concentrating all recommendations within a single local optimum. Ultimately, 10 representative low-contact-angle process conditions were selected for experimental validation. Their predictive capability was evaluated by comparing the predicted and experimentally measured contact angles using MAE, RMSE, and R^2. Importantly, these 10 samples constituted targeted experimental validation of the model-recommended region and were intended to assess whether the model could effectively identify low-contact-angle process conditions, rather than replace the independent random test set used for model evaluation.

Overall, Stage I established a complete workflow from nonlinear modeling of the existing experimental data, through expanded process-space prediction, to experimental validation using three controllable process parameters. Its primary objective was not to interpret post-wetting morphological changes, but to establish a practically useful process–wetting-performance mapping and identify potential low-contact-angle regions. The newly validated samples subsequently provided the experimental basis for incorporating final surface morphology into the Stage II analysis.

3.2 Stage II

Following the prediction, optimization, and experimental validation of the recommended process conditions

in Stage I, Stage II was developed to further investigate the relationship between the actual wetting response and the final surface morphology. Unlike Stage I, which focused exclusively on process parameters that can be determined before experimentation, Stage II incorporated three-dimensional morphological features measured after wetting, thereby providing a more comprehensive statistical description of the final wetting state while retaining the original process information.

Specifically, the 10 experimentally validated samples selected in Stage I were combined with the original 125 samples to form an expanded database containing 135 samples. Pearson correlation analysis was first performed on nine candidate features to identify highly correlated variables and reduce feature redundancy. Based on the correlation results, height range and profile kurtosis were removed. The final feature set therefore consisted of seven variables: Temperature, Ti content, nominal roughness, root-mean-square roughness (roughness_rms), profile skewness, anisotropy index, and volume proxy. This feature-selection procedure helped reduce the potential effects of multicollinearity on model training and subsequent SHAP-based feature attribution.

For model development, the 135 samples were stratified according to the target variable and divided into 94 training samples, 20 validation samples, and 21 test samples, which were used for model training, model selection, and final performance evaluation, respectively. During training, 5-fold cross-validation and hyperparameter optimization were performed exclusively within the training set to prevent information leakage from the validation and test sets. Four representative regression algorithms—LASSO, RF, XGBoost, and GBR—were compared using R^2, RMSE, and MAE on the validation set as the primary model-selection criteria. The GBR model, which achieved the best validation performance, was selected as the final model. The training and validation sets were then combined for model retraining, followed by evaluation on the 21 test samples that had not been involved in model training or selection, providing an independent assessment of model performance on the current dataset.

After the final model was established, SHAP (SHapley Additive exPlanations) was employed to interpret the GBR predictions. SHAP values calculated from the test set were used as the primary basis for generalization-oriented interpretation. The mean absolute SHAP value of each feature was used to quantify its overall contribution, while the SHAP beeswarm plot was used to examine the direction and magnitude of the effects associated with different feature values. Representative samples were also selected for local SHAP analysis to further examine the combinations of features associated with high- and low-contact-angle predictions.

Overall, Stage II extended the Stage I process–wetting prediction framework by incorporating post-wetting surface morphology, thereby establishing a multi-feature model linking “process parameters + final surface morphology” to the equivalent contact angle. Its primary purpose was not forward prediction or process-condition recommendation, but rather to statistically identify the relative contributions of process parameters and final morphological features to the observed wetting state. Accordingly, the SHAP contributions of the morphological descriptors should be interpreted as statistical associations with the final wetting state rather than as evidence of independent causal effects.

4. Results and Discussion

4.1 Stage I: Prediction and Process Optimization Based on Three Process Features

After establishing the Stage I models, the predictive performance of the different regression algorithms was systematically compared to identify the model best suited to describing the nonlinear relationship between temperature, Ti content, nominal roughness, and equivalent contact angle. The optimal model was then used to explore the expanded process space, and its recommendations were experimentally validated to assess the practical effectiveness of the machine-learning-based process optimization.

As shown in Figure 2, the results obtained from the eight regression models demonstrate a pronounced nonlinear relationship between temperature, Ti content, nominal roughness, and equivalent contact angle. The OLS model exhibited relatively limited predictive capability, whereas the Ridge-Poly2 model, which incorporates second-order terms and interaction effects, showed a substantial improvement. This indicates that low-order nonlinearities and variable interactions account for part of the wetting behavior, but are insufficient to fully capture the complex process–wetting relationship.

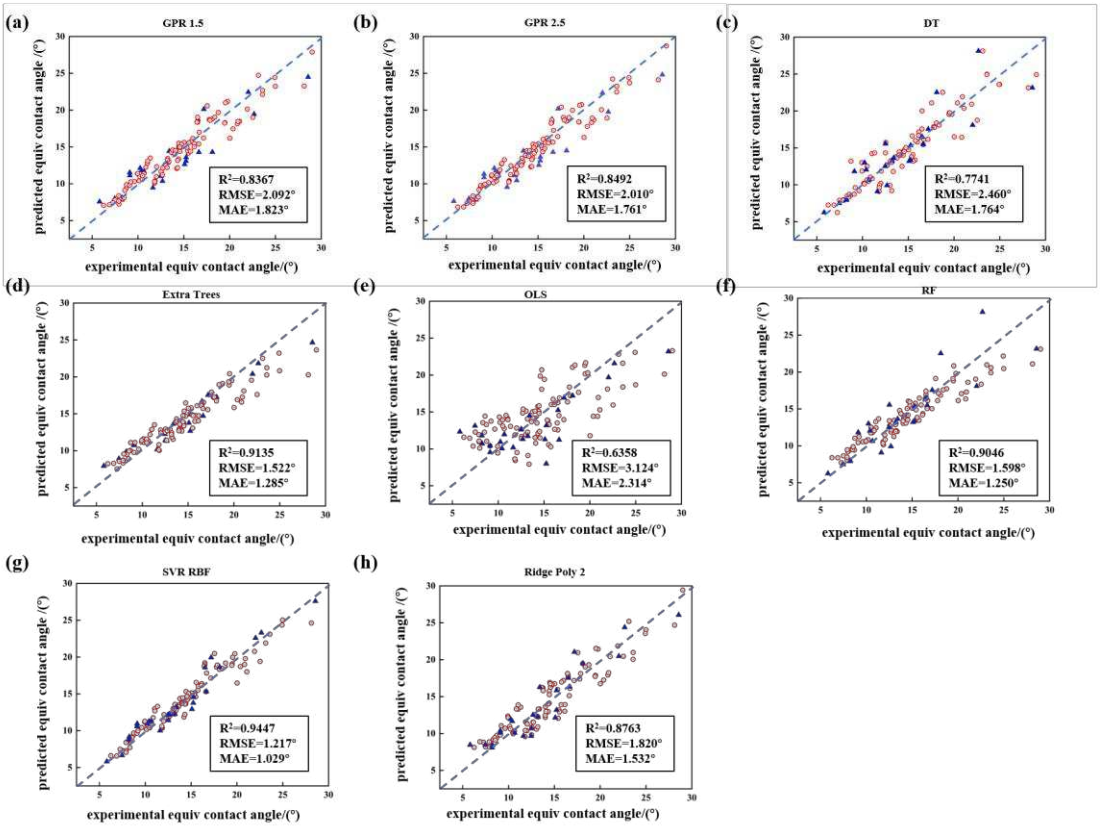

Figure 2. OOF parity plots for the eight Stage I regression models: (a) SVR-RBF, (b) Ridge-Poly2, (c) RF, (d) OLS, (e) ET, (f) DT, (g) GPR-Matérn-2.5, and (h) GPR-Matérn-1.5.

The tree-based models demonstrated a certain ability to capture nonlinear behavior, but their performance was relatively sensitive to data partitioning. For example, the DT model achieved an OOF R^2 of 0.8647, which decreased to 0.7741 on the independent test set. The test-set performance of RF and ET was further improved, although their OOF errors remained higher than those of the best-performing model. The two GPR models were also capable of capturing certain nonlinear trends, but their overall predictive performance remained inferior to that of SVR-RBF.

In contrast, SVR-RBF exhibited the best and most stable predictive performance. As shown in Figure 3, it achieved an OOF (R^2) of 0.9403, with an RMSE and MAE of 1.167° and 0.840°, respectively, under 10-fold cross-validation. On the independent test set that was not used for model training, the model achieved an (R^2) of 0.9447, with an RMSE of 1.217° and an MAE of 1.029°. The close agreement between the OOF and test-set results indicates good generalization stability, with no evident signs of overfitting. Compared with the other models, SVR-RBF provided the best balance among predictive accuracy, error magnitude, and model stability, and was therefore selected for subsequent exploration of the process design space.

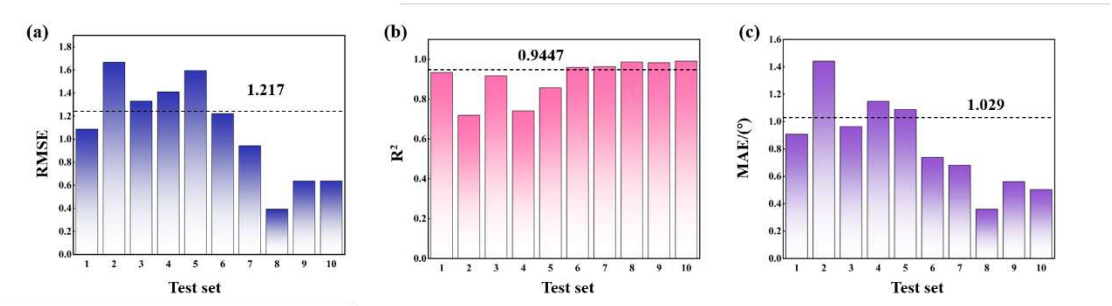

Figure 3. Independent-test parity plots for the eight Stage I regression models: (a) SVR-RBF, (b) Ridge-Poly2, (c) RF, (d) OLS, (e) ET, (f) DT, (g) GPR-Matérn-2.5, and (h) GPR-Matérn-1.5.

After identifying the optimal SVR-RBF model, it was further applied to an expanded process space beyond the original 125 experimental points to identify potential low-contact-angle regions. The expanded search comprised 37,572 candidate process conditions, with the temperature range extended to 850–950 °C, the Ti content to 2.0–4.5 wt.%, and the nominal roughness maintained at 0.075–1.50 μm. The predicted equivalent contact angles ranged from 5.21° to 31.52°, with the global minimum of 5.21° predicted at 877 °C, 3.2 wt.% Ti, and 0.30 μm nominal roughness. Notably, this optimum was located within the interior of the expanded process space rather than at its boundaries, indicating pronounced coupling among the three process variables and the existence of an internal low-contact-angle region.

Further statistical analysis of the predicted low-contact-angle conditions provided a clearer picture of the corresponding process window. The low-contact-angle conditions were mainly distributed within a temperature range of 870–890 °C, a Ti content of 3.0–3.5 wt.%, and a nominal roughness of 0.20–0.30 μm.

These results indicate that a low contact angle is not determined by the extreme value of any single process parameter, but rather by their combined process state. In particular, the minimum predicted contact angle was obtained at approximately 877 °C with 3.2 wt.% Ti and 0.30 μm roughness, suggesting the presence of a distinct local optimum in temperature rather than a simple monotonic relationship. As the temperature deviated from this region, the predicted contact angle gradually increased, while changes in Ti content and roughness also shifted the favorable temperature range. Therefore, achieving low contact angles requires an appropriate combination of temperature, Ti content, and surface roughness rather than simply increasing or decreasing an individual parameter.

Based on the distribution of the low-contact-angle region, the experimental validation did not simply select several adjacent points with the lowest predicted contact angles. Instead, 10 representative process conditions were selected from the candidate space by jointly considering the predicted contact angle, process-window coverage, and experimental feasibility, as shown in Figure 4.

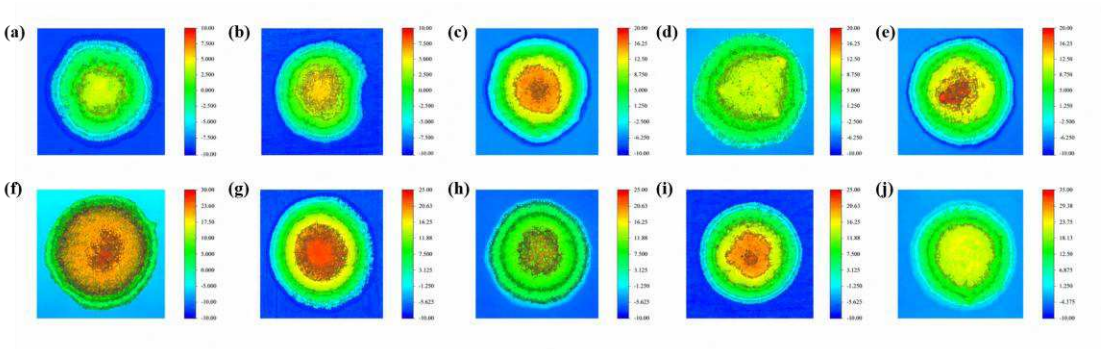

Figure 4. LSCM topography maps of the ten experimentally validated recommended specimens: (a-j) specimens 1-10.

As shown in Table 2, the 10 selected conditions covered a process range of 854–949 °C, 2.1–4.5 wt.% Ti, and 0.20–0.30 μm nominal roughness. The validation set therefore included not only conditions within the predicted optimum region but also conditions that deviated from the optimum, providing a more comprehensive assessment of the model's ability to identify the low-contact-angle region. The predicted equivalent contact angles ranged from 5.2112° to 12.1261°, compared with experimental values ranging from 5.4800° to 12.9995°. Among the 10 conditions, the predicted values were lower than the experimental measurements for six cases and higher for four cases. The mean signed error was −0.2054°, indicating only a slight overall tendency toward underprediction, with no pronounced systematic bias.

Table 2. Process parameters and predicted equivalent contact angles for the ten recommended conditions.

Specimen	Temperature (°C)	Ti content (wt.%)	Nominal roughness (μm)	Predicted equivalent contact angle (°)
1	877	3.2	0.300	5.211
2	874	3.2	0.300	5.281
3	854	3.1	0.300	8.052
4	877	3.8	0.300	8.192
5	877	2.6	0.300	8.212
6	906	3.2	0.300	9.307
7	875	4.5	0.200	9.662
8	933	3.2	0.200	10.717
9	949	3.2	0.200	10.717
10	879	2.1	0.300	12.126

In summary, the Stage I model comparison demonstrated that SVR-RBF can effectively capture the complex nonlinear relationships between the three process parameters and the equivalent contact angle, while maintaining high predictive accuracy on the independent test set. The expanded design-space search further revealed that the low-contact-angle region is not confined to a single optimum point but instead forms a localized process window centered around a moderate Ti content, a nominal roughness of 0.30 μm, and a temperature of approximately 877 °C. Within this region, conditions of approximately 870–890 °C, 3.0–3.5 wt.% Ti, and 0.20–0.30 μm roughness can be regarded as the core low-contact-angle process window predicted by the model. Subsequent targeted validation using 10 experimentally tested conditions confirmed the model's capability to accurately

identify and recommend favorable low-contact-angle regions. Consequently, Stage I established a complete closed-loop workflow encompassing experimental data modeling, design-space exploration, low-contact-angle window identification, and experimental validation, while also providing an expanded experimental dataset for Stage II, where final surface morphology features were incorporated to further interpret wetting behavior.

4.2 Stage II: Seven-Feature Machine Learning Modeling and SHAP Interpretation Using 135 Samples

Following the completion of process-parameter prediction, low-contact-angle process-window identification, and experimental validation in Stage I, the validation samples were incorporated into the analysis, together with three-dimensional surface morphology features measured after wetting, to investigate the statistical explanatory role of the final surface state in predicting the equivalent contact angle. Unlike Stage I, which focused on the prediction and optimization of experimentally controllable process conditions, Stage II aimed to characterize the predictive information contained in both process parameters and final surface morphology, and to compare their relative contributions to the final wetting state. This analysis therefore complements the process-parameter-based prediction established in Stage I.

First, Pearson correlation analysis was performed on the nine candidate features in the expanded database, with ($|r| \geq 0.7$) adopted as the criterion for strong correlation. As shown in Figure 6, the analysis identified three pairs of strongly correlated features, indicating a degree of information overlap among the morphology descriptors. To reduce feature redundancy and potential multicollinearity in model training and feature interpretation, height_range and profile_kurtosis were removed. The final feature set comprised seven input features, including three process variables—Temperature, Ti content, and nominal roughness—and four post-wetting surface morphology features: roughness rms, profile skewness, anisotropy index, and volume proxy.

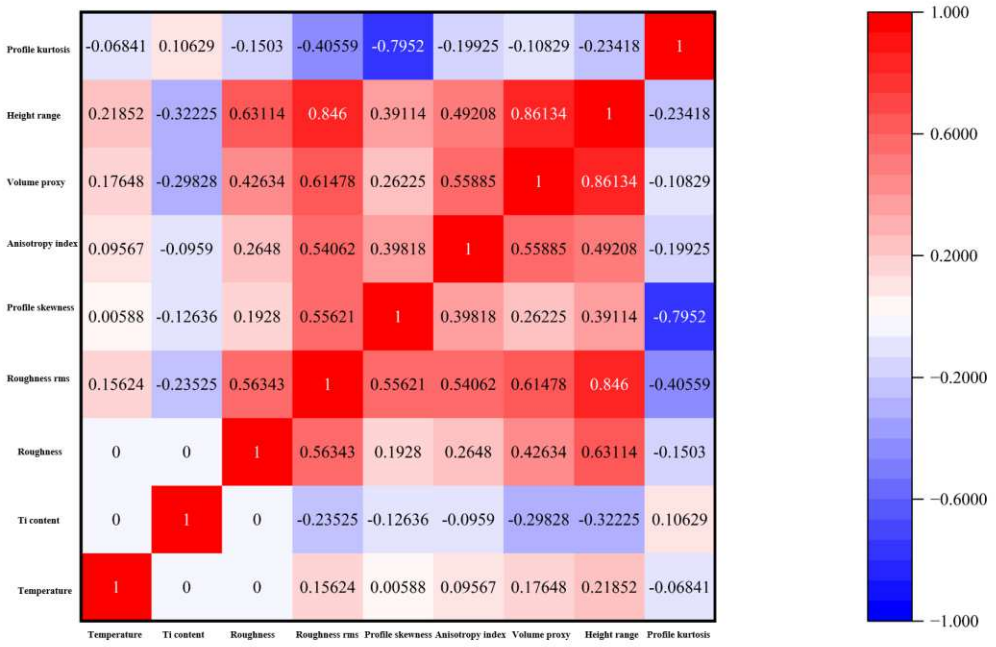

Figure 6. Pearson correlation matrix for the nine candidate features before removal of height range and profile

kurtosis.

This feature-selection procedure retained the key process and surface morphology information while reducing the interference of highly correlated variables with model training and SHAP contribution allocation. It should be emphasized that all four morphology features were obtained from the final surface after wetting. Therefore, they were used primarily to characterize and interpret statistical differences in the final wetting state, rather than as independently controllable process variables available prior to experimentation. Accordingly, their contributions should not be interpreted as establishing a strict temporal or causal relationship.

After determining the seven input features, the Stage II models were trained and compared using the 135 samples in the expanded database. The dataset was divided into training, validation, and test sets containing 94, 20, and 21 samples, respectively. The training set was used for model fitting and cross-validation, the validation set for model selection, and the final test set for evaluating the independent generalization performance of the selected model. As shown in Table 3, comparison of the four regression models—LASSO, RF, XGBoost, and GBR—revealed a clear performance difference between the linear model and the nonlinear ensemble models. LASSO and RF achieved validation-set (R^2) values of 0.7854 and 0.7786, respectively, whereas XGBoost and GBR reached 0.9554 and 0.9667, respectively, as shown in Figure 7. These results indicate that, even when both process parameters and final surface morphology are considered, the equivalent contact angle retains strong nonlinear relationships and feature interactions with the input variables, which cannot be adequately captured by a simple linear model. GBR achieved the highest validation-set (R^2) and was therefore selected as the final model.

Table 3. Validation and held-out test performance of the four Stage II regression models.

Model	Validation R^2	Validation RMSE (°)	Validation MAE (°)	Test R^2	Test RMSE (°)	Test MAE (°)
LASSO	0.7854	2.1947	1.8038	0.7471	2.1639	1.7598
RF	0.7786	2.2292	1.6905	0.8141	1.8549	1.4380
XGBoost	0.9554	1.0003	0.7834	0.9132	1.2675	0.8121
GBR	0.9667	0.8648	0.6653	0.9214	1.2061	0.8278

Subsequently, the training and validation sets were combined, and the GBR model was refitted using all 114 samples. The refitted model was then independently evaluated on the 21 test samples that had not been used for either model training or model selection. As shown in Figure 7, the GBR model achieved a test-set ($R^2 = 0.9214$), RMSE = 1.2061°, and MAE = 0.8278°, indicating that it retained good predictive capability. Although a certain difference in performance was observed between the validation and test sets, the overall predictive accuracy remained high. These results demonstrate that, by incorporating both process parameters and final surface morphology features, the GBR model can effectively capture the complex nonlinear relationships between these features and the final equivalent contact angle.

After establishing the final GBR model, SHAP analysis was further employed to quantify the contribution of each feature to the prediction of the equivalent contact angle. The global mean absolute SHAP values were calculated based on the 21 test samples and subsequently normalized. The results ranked the features in descending order of importance as follows: roughness (27.52%), Ti content (21.86%), Temperature (20.93%), roughness rms (13.32%), volume proxy (7.68%), anisotropy index (5.54%), and profile skewness (3.15%). The three process

variables accounted for a combined contribution of 70.31%, confirming that they remained the primary sources of predictive information. In contrast, the four post-wetting surface morphology features contributed 29.69% in total. Among them, roughness rms showed the highest contribution, indicating a relatively strong statistical association between the final surface height variation and the wetting state. Volume proxy, anisotropy index, and profile skewness contributed 7.68%, 5.54%, and 3.15%, respectively, providing complementary information for characterizing the final wetting state.

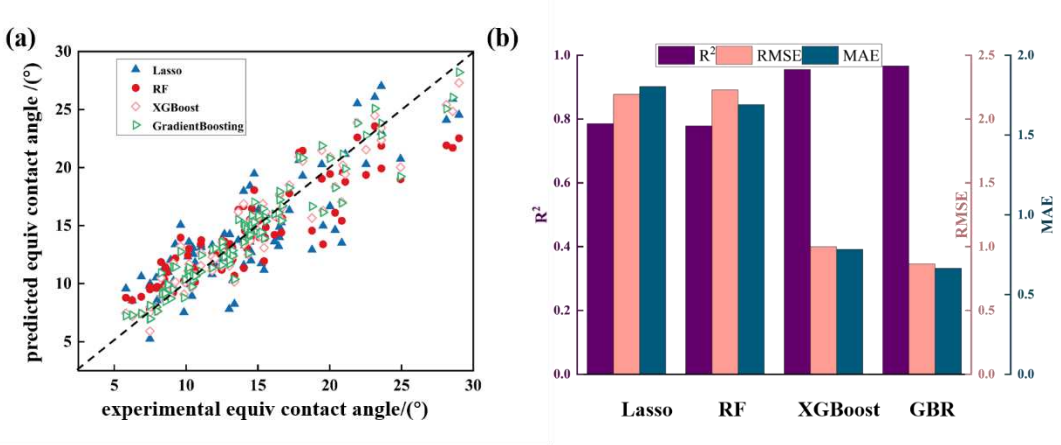

Figure 7. Stage II model comparison: (a) experimental versus predicted equivalent contact angles for the four models and (b) comparison of validation-set R^2, RMSE, and MAE.

As shown in Fig. 8, Fig. 8(a) presents the global mean absolute SHAP values and importance ranking of the input features, enabling a direct comparison of their relative contributions to the model predictions. Fig. 8(b) further illustrates the direction and magnitude of the effects of different feature values on the predicted equivalent contact angle using a SHAP beeswarm plot, indicating nonlinear relationships between the input features and the model output. Fig. 8(c) compares the experimental and GBR-predicted values for the test set. The data points are generally distributed close to the (y=x) reference line, demonstrating good agreement between the predictions and experimental measurements. Fig. 8(d) shows the absolute prediction errors for the 21 test samples, with most samples exhibiting relatively small errors and only a few showing comparatively larger deviations.

Overall, Fig. 8 demonstrates the effectiveness of the GBR model in terms of both predictive accuracy and feature interpretation. The model provides accurate predictions of the equivalent contact angle, while the SHAP analysis confirms that the three process variables are the dominant sources of predictive information and that the four post-wetting morphology features provide additional explanatory value.

The Stage II results therefore do not imply that post-wetting morphology features play a minor role; rather, their role differs fundamentally from that of the process variables. The process variables provide information on the controllable conditions prior to wetting, whereas the four morphology descriptors provide complementary information on the surface state established after wetting. Collectively, the morphology features account for nearly 30% of the model's predictive information, indicating that although temperature, Ti content, and nominal roughness can provide relatively accurate predictions of the equivalent contact angle, they cannot fully capture the variations in the final state produced during the wetting process. In particular, the relatively high contributions of roughness rms and volume proxy suggest that height variation and spatial morphological characteristics of the final surface may provide valuable information for interpreting differences in wetting behavior.

These findings are consistent with the process-based predictions obtained in Stage I. Stage I demonstrated

that temperature, Ti content, and nominal roughness could predict the equivalent contact angle with high accuracy. Stage II further shows that, after incorporating post-wetting morphology features, the three process variables remain dominant, while the final surface morphology contributes approximately 29.69% of the predictive information. This indicates that the wetting outcome is associated not only with the initial process conditions but also with the actual surface state formed after wetting. However, because these morphology features were measured after wetting, the SHAP results should be interpreted as reflecting predictive associations and explanatory value, rather than as evidence that these morphological parameters exert independent causal effects on wetting behavior.

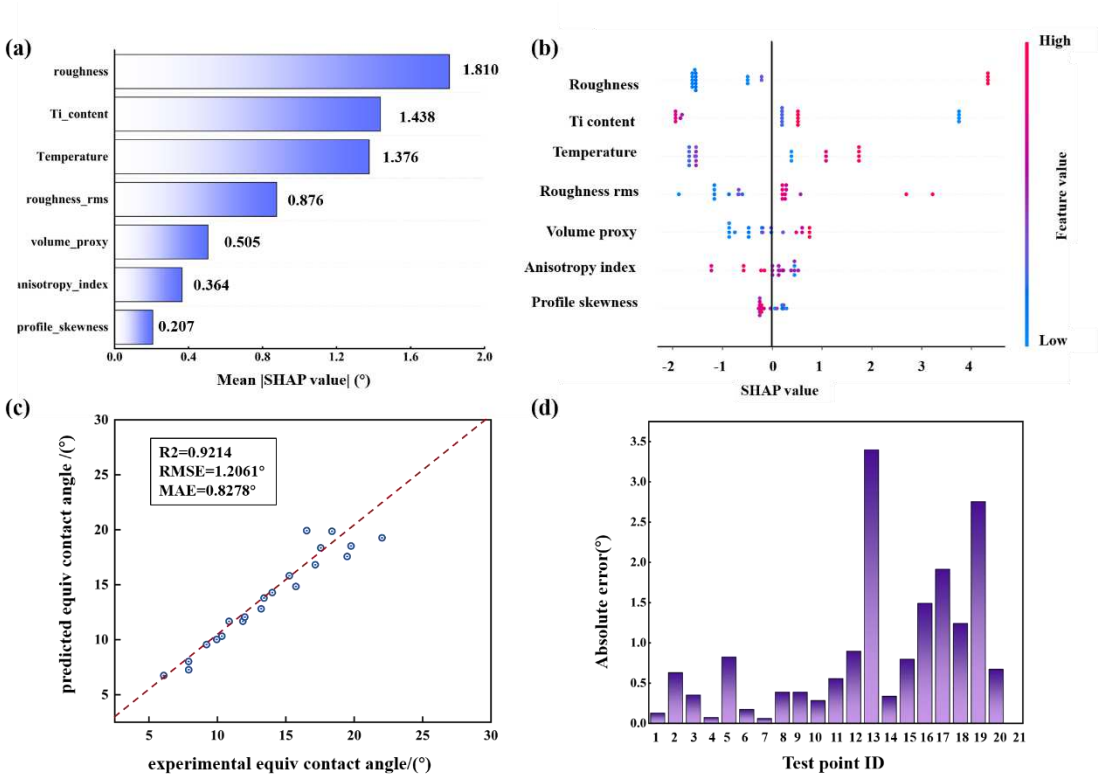

Figure 8. Tree SHAP beeswarm plot for the final GBR model evaluated on the 21-sample held-out test set.

In summary, the Stage II analysis demonstrates that the seven features retained after correlation-based screening provide an effective representation of the wetting state in the expanded experimental dataset, with the GBR model achieving strong predictive performance on both the validation and independent test sets. SHAP analysis identifies roughness, Ti content, and Temperature as the three most influential features, collectively accounting for 70.31% of the total feature contribution. Meanwhile, the four post-wetting surface morphology features—roughness rms (13.32%), volume proxy (7.68%), anisotropy index (5.54%), and profile skewness (3.15%)—contribute a combined 29.69%, demonstrating that the final surface morphology provides important complementary information beyond the process parameters. Thus, Stage II not only confirms the dominant role of the process variables but also highlights the additional explanatory value of the final surface morphology for predicting the equivalent contact angle, providing a basis for discussing the statistical associations among process conditions, final surface morphology, and wetting state.

5. Conclusions

This study investigated the wetting behavior of the WCu/AgCuTi brazing system through experiments and

machine learning, and established a two-stage analytical framework integrating process prediction, process optimization, and final-state interpretation. In Stage I, temperature, Ti content, and nominal roughness were used as input variables, with the equivalent contact angle as the response. Comparison of multiple regression models demonstrated that SVR-RBF provided the best predictive performance, achieving a test-set (R^2 = 0.9447), RMSE = 1.217°, and MAE = 1.029°. Based on this model, 37,572 expanded process combinations were screened, yielding a minimum predicted contact angle of 5.21° at 877 °C, 3.2 wt.% Ti, and 0.30 μm nominal roughness. Further analysis showed that low-contact-angle conditions were mainly concentrated within approximately 870–890 °C, 3.0–3.5 wt.% Ti, and 0.20–0.30 μm, which can be regarded as the core low-contact-angle process window predicted by the model. Experimental validation of 10 recommended conditions yielded an (R^2 = 0.9105), MAE = 0.5513°, and RMSE = 0.6319°, confirming the model's ability to identify and recommend low-contact-angle regions.

In Stage II, the dataset was expanded to 135 samples by incorporating post-wetting three-dimensional surface morphology features. The final GBR model achieved (R^2 = 0.9214), RMSE = 1.2061°, and MAE = 0.8278° on the independent test set. SHAP analysis identified nominal roughness, Ti content, and temperature as the three most influential features, collectively accounting for 70.31% of the total contribution. Meanwhile, the post-wetting morphology features—roughness rms (13.32%), volume proxy (7.68%), anisotropy index (5.54%), and profile skewness (3.15%)—contributed a combined 29.69%, demonstrating that the final surface morphology provides important complementary information beyond the initial process parameters. Overall, this study establishes a complete workflow from process-parameter prediction — low-contact-angle process-window identification — experimental validation — final-morphology interpretation, and demonstrates the importance of combining moderate Ti content, an appropriate brazing temperature, and low-to-moderate surface roughness for achieving favorable wetting performance.

Author contribution

Xinmei Zhang: conceptualization, writing—original draft, formal analysis, visualization, software. XingXing Wang: conceptualization, methodology, writing—review and editing, revise, supervision. Shuai Wang: writing—review and editing, supervision. Jianjun Shi: writing—review and editing, supervision. Huawei Sun: writing—review and editing, supervision. Huawei Sun: writing—review and editing, supervision. ZhiPeng Yuan: writing—review and editing, supervision.

Declaration of competing interest

The authors declare that they have no known competing financial interests or personal relationships that could have appeared to influence the work reported in this paper.

Acknowledgments

This research was financially supported by National Natural Science Foundation of China (52475347), Key Research and Development Projects in Henan Province (251111222600), the Science and Technology Innovation Leading Talent Support Program of Henan Province (254200510047), and Research Special Program under the Key Scientific Research Project Plan of Institutions of Higher Education in: Henan Province (26ZX018).

References

[1] Akkaya, I., O. Arslan, and J.P. Rolland, Automated and highly precise surface wetting contact angle measurement with optical coherence tomography based on deep learning model. Measurement, 2025.

253.

[2] Fang, J., et al., Optimized design of composition and brazing process for Cu-Ag-Zn-Mn-Ni-Si-B-P alloy brazing material based on machine learning strategy to improve brazing properties. Materials Today Communications, 2024. **39**.

[3] Fu, J., et al., Wettability prediction and feature importance analysis for laser-chemical induced superwetting surface based on machine learning. Journal of Manufacturing Processes, 2025. **152**: p. 57-67.

[4] Fushun, X., et al., Morphology Development and Kinetics of Plate or Rod Shaped Precipitates in Aluminum Alloys. Rare Metal Materials and Engineering, 2017. **46**(4): p. 876-881.

[5] Li, Y., et al., Wetting and spreading of AgCuTi on Fe substrate at high temperatures: A molecular dynamics study. Journal of Materials Research and Technology, 2023. **27**: p. 5783-5790.

[6] Zhang, Z., et al., Wetting kinetics of TixMo1-xC in molten Fe and its influence on bicontinuous TixMo1-xC/Fe composite mechanics: Experimental, DFT and ML studies. Journal of Materials Research and Technology, 2024. **30**: p. 295-306.

[7] Zhao, S., et al., Mechanism of wettability enhancement of the AgCuTi-SiO2f/SiO2 system with a laser-manufactured bioinspired sinusoidal interface. Journal of Manufacturing Processes, 2026. **157**: p. 808-825.

[8] Li, Z., et al., First-principles calculations of the effects of the interface microstructure on the wettability of a Cu–Ti/AlN system. Ceramics International, 2021. **47**(13): p. 18592-18601.

[9] Lin, W., et al., Effect of brazing temperature on the microstructure and mechanical properties of diamond/kovar joints. Diamond and Related Materials, 2025. **159**.

[10] Liu, D.-G., et al., Microstructure, mechanical properties and hermeticity of W-Cu/HTCC brazed joints with surface metallization. International Journal of Refractory Metals and Hard Materials, 2024. **118**.

[11] Qiang, X., et al., Effect of Ti content on the microstructure and properties of Sc2W3O12 particle-reinforced Ag-Cu-Ti brazing alloy joints for brazing SiC and Cu. Materials Today Communications, 2025. **47**.

[12] Wang, P., et al., Unrevealing the wetting behavior and mechanism of AgCuTi filler on negative thermal expansion Sc2W3O12 materials: Experiments and First-principles calculations. Applied Surface Science, 2024. **652**.

[13] Wang, P., et al., Investigate the effect of C coating on the wetting and reaction mechanism of Sc2W3O12 and AgCuTi filler. Materials Characterization, 2024. **211**.

[14] Wen, Y., et al., Effect of Ti content on microstructure and properties of Cu/AgCuTi/Al2O3 brazed joints. Materials Today Communications, 2024. **40**.

[15] Wu, H., et al., Microstructure and mechanical properties of single-crystal diamond/Kovar alloy joints brazed with an AgCuTi metal filler. Diamond and Related Materials, 2023. **138**.

[16] Wu, J., et al., Vacuum brazing-induced dissolutive mechanisms in AgCuTi/Cu system. Materials Letters, 2025. **395**.

[17] Wu, M., et al., Effects of roughness on the wettability of high temperature wetting system. Surface and Coatings Technology, 2016. **287**: p. 145-152.

[18] Xin, C., et al., Effects of Ti content on the wetting behavior and chemical reaction in AgCuTi/SiO2 system. Vacuum, 2019. **167**: p. 152-158.

[19] Xu, H., et al., The influence of Ti content in AgCuTi filler on its wetting and spreading mechanism on silicon nitride ceramics: An experiment and first-principles calculation study. Materials Today Communications, 2024. **41**.

[20] Yao, W., et al., Effects of brazing parameters on interfacial reaction layer characteristics and mechanical performance of brazed Cu/Si3N4 using Ag-Cu-Ti filler alloy. Materials Science and Engineering: A,

2025. **936**.

[21] Xu, H., et al., Investigation on wetting behavior and mechanism of AgCu-Xwt.%Ti filler metal/AlN ceramic reactive wetting system: Experiments and first-principles calculations. Journal of Alloys and Compounds, 2021. **869**.